Multivariate Statistical Integration of Satellite Infrared and Microwave Radiometric Measurements for Rainfall Retrieval at the Geostationary Scale

Frank Silvio Marzano, *Senior Member, IEEE*, Massimo Palmacci, Domenico Cimini, *Member, IEEE*, Graziano Giuliani, and Francis Joseph Turk, *Member, IEEE*

Abstract—The objective of this paper is to investigate how the complementarity between low earth orbit (LEO) microwave (MW) and geostationary earth orbit (GEO) infrared (IR) radiometric measurements can be exploited for satellite rainfall detection and estimation. Rainfall retrieval is pursued at the space–time scale of typical geostationary observations, that is at a spatial resolution of few kilometers and a repetition period of few tens of minutes. The basic idea behind the investigated statistical integration methods follows an established approach consisting in using the satellite MW-based rain-rate estimates, assumed to be accurate enough, to calibrate spaceborne IR measurements on sufficiently limited subregions and time windows. The proposed methodologies are focused on new statistical approaches, namely the multivariate probability matching (MPM) and variance-constrained multiple regression (VMR). The MPM and VMR methods are rigorously formulated and systematically analyzed in terms of relative detection and estimation accuracy and computing efficiency. In order to demonstrate the potentiality of the proposed MW–IR combined rainfall algorithm (MICRA), three case studies are discussed, two on a global scale on November 1999 and 2000 and one over the Mediterranean area. A comprehensive set of statistical parameters for detection and estimation assessment is introduced to evaluate the error budget. For a comparative evaluation, the analysis of these case studies has been extended to similar techniques available in literature.

Index Terms—Data fusion, infrared radiometry, microwave radiometry, rainfall estimation, satellite meteorology, sensor synergy.

I. INTRODUCTION

THE ACCURATE retrieval of surface rain rate (RR) from spaceborne remote sensing systems on a global scale with high temporal and spatial resolutions is one of the major goals of current scientific research [1]–[3]. Satellite-based methodologies can offer several advantages with respect to ground-based techniques. The latter, such as those using rain gauges and radars, generally suffer from spatial coverage problems. Rain gauge measurements, subject to errors due to evaporation and surface winds, can only supply cumulative point estimates for limited areas (e.g., [4] and [5]). On the other hand, ground-based radar systems can provide fairly continuous coverage in space and time, but their spatial coverage is generally limited to few hundreds of kilometers and phenomena, such as beam filling, anomalous propagation, or bright band in stratiform clouds, must be faced with any radar measurement of rainfall (e.g., [6]–[8]). Most importantly, both rain gauges and radars provide incomplete coverage on a global scale, particularly over the oceans where such instruments are sparse or nonexistent.

As an alternative solution, rainfall measurement from satellites has been an active field of study. However, the problem of using satellite remote sensing data appears to be fairly complicated, since presently there is not a single spaceborne platform that can carry all the suitable instruments to ensure all the above-mentioned properties to the rainfall product [9]–[12]. From a meteorological point of view, visible (VIS) and infrared (IR) radiometers can give information on cloud top layers due to their high albedo at optical wavelengths and IR equivalent-blackbody brightness temperatures (T_{IR}) almost equal to cloud physical temperature (e.g., [13] and [14]). On the other hand, microwave (MW) radiometers can detect cloud structure and rain rate, since MW brightness temperatures (T_B's) are fairly sensitive to liquid and ice hydrometeors (e.g., [15]–[17]). Regarding platforms, geosynchronous earth orbit (GEO) satellites can ensure a coverage with a high temporal sampling (order of half an hour) from a flight altitude of about $36\,000$ km, while low earth orbit (LEO) satellites have the advantage to fly at a lower altitude (from 400–800 km), thus enabling the use of microwave sensors without losing too much in spatial resolution (order of kilometers to tens of kilometers). The major drawback of LEOs is the low temporal sampling, only twice a day in a given place at midlatitude [1], [2]. Therefore, LEO–MW and GEO–IR radiometry are clearly complementary for monitoring the earth's atmosphere and a highly variable phenomenon such as precipitation [18]–[23].

Statistical integration of satellite IR and microwave data can be accomplished in several ways. On one hand, there is a choice of what variables (i.e., predictors) to match in order to provide the final product. A possibility is represented by the direct combination of nearly instantaneous MW T_B's and IR T_{IR}'s, having the advantage to exploit the observable information without any postprocessing and the disadvantage to request IR

F. S. Marzano and G. Giuliani are with the Center of Excellence on Remote Sensing and Hydro-Meteorological Modeling (CETEMPS) and the Department of Electrical Engineering, University of L'Aquila, 67070 L'Aquila, Italy (e-mail: marzano@ing.univaq.it).

M. Palmacci and D. Cimini are with the Department of Electrical Engineering, University of L'Aquila, 67040 L'Aquila, Italy.

F. J . Turk is with the Marine Meteorology Division, Naval Research Laboratory, Monterey, CA 93940 USA.

and MW measurements matched in space and time. However, the latter condition is only satisfied a limited number of times in a given area if few LEO platforms are considered, thus flaring the potentiality of setting up a rapid-updating retrieval algorithm. The feasible approach would be that based on physically based combined retrieval algorithms which, on the other hand, would need a climatological and microphysical tuning (e.g., [5] and [24]).

In order to avoid these difficulties, one can resort to approaches that aim to combine IR measurements and MW-based estimates on a statistical basis. By properly choosing a space–time resolution, the ergodicity of the rain process and satellite observations can be invoked. The inversion algorithm, i.e., retrieving rain rate from IR data, can be then derived by using statistical regression or probability matching of the involved variables (or corresponding statistical moments) [6], [25]. Even though less physical, the statistical matching exhibits several peculiar features that can be easily exploited for an operational global-scale approach. Indeed, artificial neural networks can be conveniently applied to the same problem dealing with empirically trained algorithms showing comparable performances [26], [27].

In this paper, a systematic analysis of statistical integration methods is carried out in order to use MW-based rain-rate estimates to calibrate IR measurements. It is worth mentioning that the emphasis is not on the rain-rate estimate validation (investigated elsewhere [28]), but on the testing and verification of MW and IR data fusion techniques to reproduce MW-derived RR fields, assumed as "ground truth." Here, we limit our interest to the use of microwave radiometric data, derived from the Special Sensor Microwave Imager (SSM/I) aboard the Defense Meteorological Special Program (DMSP) satellites and from the TRMM Microwave Imager aboard the Tropical Rainfall Measuring Mission (TRMM) satellite coupled with data from the Visible Infrared Spinning Scan Radiometer (VISSR) aboard MeteoSat satellites. Satellite-based passive MW data exhibit the unique feature of a global-scale availability with a relatively low cost and increasing number of platforms. A generalization of the proposed techniques to rain-rate estimates, derived from not only other spaceborne sensors such as the Precipitation Radar (PR) on TRMM and the Advanced Microwave Scanning Unit (AMSU) on National Oceanic and Atmospheric Agency (NOAA) satellite, the Advanced Microwave Scanning Radiometers (AMSR) aboard EOS-Aqua and ADEOS-II satellites, but also from both rain gauges and ground-based radars (e.g., [18], [20], and [29]), is almost straightforward. In case of a multisatellite MW radiometer constellation, the issue of rain-rate product consistency has to be faced in order to ensure at least a statistical homogeneity.

The proposed MW–IR combined rainfall algorithm (MICRA) is based on the statistical integration of collocated GEO–IR and LEO–MW data, accomplished on a global scale using an ensemble of subregions, partially overlapped. This time–space segmentation permits also to analyze stationarity and homogeneity statistical properties of the precipitation random process. New techniques, named multivariate probability matching (MPM) and variance-constrained multiple regression (VMR), are investigated in terms of relative estimate

accuracy, algorithm parameter sensitivity, cloud classification impact, and computing efficiency. Similar techniques, available in literature, are also considered for comparison. As an application, some case studies on a local and global scales are finally discussed, in order to demonstrate the potentiality of monitoring rainfall attenuation and precipitation using the proposed statistical integration techniques.

II. STATISTICAL INTEGRATION TECHNIQUES

The general idea behind the MICRA considered statistical integration techniques is to combine the appealing spatial and temporal sampling of IR sensors, mounted on geostationary platforms, with the higher accuracy of passive MW methods for of rain-rate retrieval. The statistical integration techniques are applied within a procedure which is supposed to run continuously on global scale. This procedure is based on a *background process* and a *foreground process*. Both the block diagram and the temporal flowchart of MICRA are schematically sketched in Fig. 1.

The *background process* consists first in estimating the surface rain rate from available LEO–MW measurements by means of either empirical retrieval algorithms (e.g., [30] and [31]) or inversion schemes based on parametric cloud radiative models (e.g., [5], [10], [16], and [24]) (*inversion step*). This means that we are considering an estimator F^{-1} that enables the inversion a set of T_B's at frequency ν_n and polarization p_m, generally spanning from 10–50 GHz and two linear orthogonal polarizations for rainfall applications, to provide a rain-rate product spatially integrated within the nominal area A. In an explicit form, it can be stated that

$$R = F^{-1}\left[T_B(\nu_1, p_1), T_B(\nu_1, p_2), \ldots, \right.$$
$$\left. T_B(\nu_N, p_1), T_B(\nu_N, p_2)\right] \quad (1)$$

where N is the number of frequencies for two polarizations p_1 and p_2. Notice that the field of views of satellite T_B's are frequency dependent (ranging from 60 km down to a few kilometers), and the estimation accuracy over land may be largely worse than over ocean [32]. On the other hand, as already said, the estimator can include any type of rainfall measurement both from space and from the ground.

The second step of the background process pursues the combination of LEO–MW sensor data with data coming from GEO–IR sensor in space and time on a global scale (*collocation step*). The first step of the background process is to locate temporally the GEO–IR data within the past few tens of minutes of the LEO–MW data time and to remap into the geographic coordinates both GEO–IR and LEO–MW measurements available observations. Note that since spatial resolution of MW data is generally worse than IR ones, a MW field of view of nominal area A generally includes more than one IR pixel. For DMSP-SSM/I products, for instance, the nominal resolution of 25 km corresponds at midlatitudes at about 5 × 5 pixels of the MeteoSat-VISSR IR channel [21], [33]. Thus, for a given MW-based rain rate R, attributed to a nominal area A, we can compute several spatial moments of IR brightness temperature T_{IR}: 1) average value T_a within
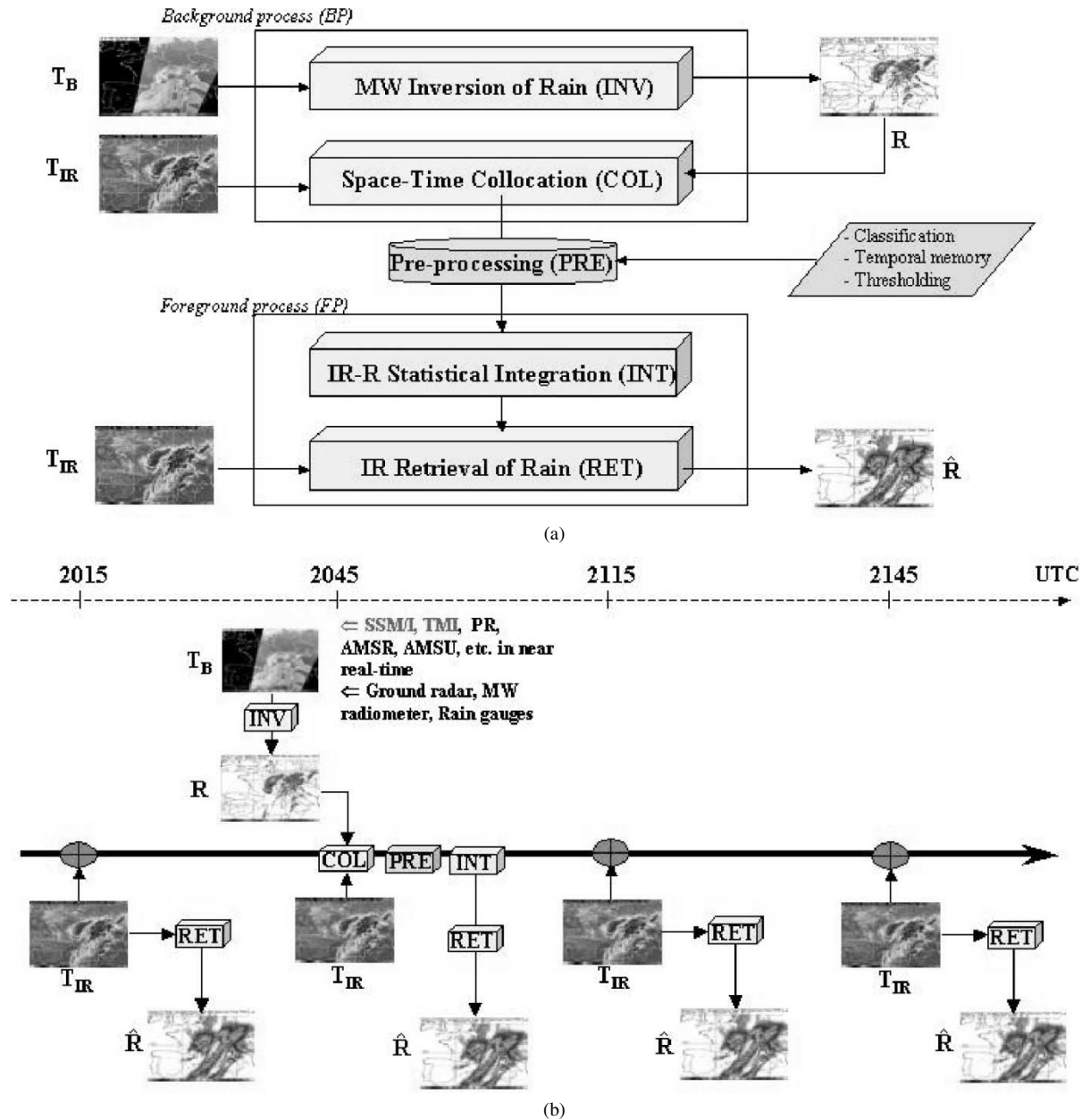
(a)

(b)

Fig. 1.   (a) Block diagram of MICRA. T_B and T_{IR} indicate MW and IR brightness temperature, respectively, while R and $\hat{R}$ indicate the MW-based and IR-based estimate of rain rate, respectively. (b) Temporal flow diagram of MICRA.

A; 2) minimum value T_m within A; 3) standard deviation σ_T within A. If N_A represent the IR pixels within the nominal area A, a numerical evaluation of previous quantities is given by

$$T_a \cong \frac{1}{N_A} \sum_{l=1}^{N_A} T_{IRl}$$

$$\sigma_T \cong \sqrt{\frac{1}{N_A - 1} \sum_{l=1}^{N_A} (T_{IRl} - T_a)^2}$$

$$T_m = \min_A [T_{IR}] \qquad (2)$$

where $\min_A$ is the minimum operator within A. The inclusion of T_m and σ_T, besides T_a, can give an information of spatial texture of IR field within the nominal area A.

As a result of the background process, a dataset is generated, containing the per-pixel rain rate retrieved from LEO–MW data,

the colocated GEO–IR brightness temperature, and the pixel geolocation. This process is continuously ongoing, since new LEO–MW and GEO–IR data are continuously ingested on a global scale depending on available satellite platforms. A *pre-processing* stage, which will be described in the next section, is accomplished after each background process as illustrated in Fig. 1.

A *foreground process* is started to derive the R–T_{IR} inverse relationship once the dataset has been updated, as shown in Fig. 1(b). The entire globe is divided in *subregions S* which are equally sized (by $\alpha \times \alpha$ degrees) and spaced (by β degrees). The parameter α is generally chosen larger than β in order to assure a smooth transition between adjacent subregions. The IR retrieval relationships are updated every time a new set of combined data have been added to the dataset relative to that subregion and are derived using data archived in a time window of several hours

(*integration step*). As a matter of fact, to assure that only the most recent rain history is captured and to guarantee a statistical significance of the training set, the R–T_{IR} inverse relationship for a given subregion is derived using only the most recent combined data. The last step is represented by the prediction of the surface rain rate from IR measurements in a given subregion by applying the derived R–T_{IR} algorithm (*retrieval step*).

As already mentioned, many attempts have been carried out so far to derive this R–T_{IR} relationship, using different techniques such as probability matching formulations, regression methods and artificial neural networks. In the next paragraphs, the new statistical methods will be illustrated. In the next two sections, some details on the implemented background and foreground processes will be given together with the discussion of case studies.

A. MPM

The probability matching criterion was first introduced in radar meteorology to derive rain-rate estimates from radar reflectivity measurements [6]–[8]. Its extension to satellite rain measurements is almost straightforward, even though some deductions ought to be derived with caution.

The basic idea behind the probability matching technique is to derive the inverse relationship between measured IR data and rain rate using the corresponding histograms of the occurrences of R and the average value T_a. If p_R and p_{Ta} are the probability density functions (pdfs) of R and T_a, respectively, we can translate this concept by the following equality:

$$p_R(R)dR = p_{Ta}(T_a)dT_a. \tag{3}$$

There is a theoretical and experimental evidence that the correlation between R and T_a is basically negative, i.e., $c(R, T_a) < 0$. This indicates that higher rain rates are associated to lower IR brightness temperatures due to the increasing cloud opacity and top height [13], [14]. Moreover, both R and T_a are positive defined. Thus, the probability matching functions can be written from (3) as

$$P_R(R \le \hat{R}) = P_{Ta}(T_a \ge \widetilde{T}_a) = 1 - P_{Ta}(T_a \le \widetilde{T}_a) \tag{4}$$

where P_R and P_{Ta} are the cumulative distribution functions (cdfs) or probabilities of R and T_a, respectively, $\hat{R}$ is the estimated value of rain rate, and $\widetilde{T}_a$ is the IR measured average value of T_{IR}. By considering the sensitivity of any MW-based rainfall estimation, a minimum nonnull value R_0 of R will correspond the (maximum) threshold value T_{a0} of T_a so that

$$\int_0^{R_0} p_R(R)dR = \int_{T_{a0}}^{\widetilde{T}_a} p_{Ta}(T_a)dT_a. \tag{5}$$

From (5) and (4), the univariate probability matching (UPM) can be stated as

$$\int_{R_0}^{\hat{R}} p_R(R)dR = \int_{\widetilde{T}_a}^{T_{a0}} p_{Ta}(T_a)dT_a$$

$$= \int_0^{T_{a0}} p_{Ta}(T_a)dT_a - \int_0^{\widetilde{T}_a} p_{Ta}(T_a)dT_a. \tag{6}$$

From (6), the retrieval relation $\hat{R} = f_U(\widetilde{T}_a)$ can be easily derived. Some details on the implementation aspects will be given later on.

In order to extend the UPM technique to the multivariate case, it is opportune to transform (6) into a formally easier form by setting

$$t_a \equiv T_{a0} - T_a. \tag{7}$$

By noting that now $c(R, t_a) > 0$, i.e., there is a positive correlation between R and the transformed variable t_a, and it holds

$$p_{Ta}(T_a)dT_a = p_{ta}(t_a)dt_a \tag{8}$$

the general expression (6) can be transformed into

$$\int_{R_0}^{\hat{R}} p_R(R)dR = P_R(R \le \hat{R}) = \int_0^{\widetilde{t}_a} p_{ta}(t_a)dt_a = P_{ta}(t_a \le \widetilde{t}_a) \tag{9}$$

where P_{ta} is the cdf of t_a, $\widetilde{t}_a = T_{a0} - \widetilde{T}_a$, and it holds $p_{ta}(t_a) = -p_{Ta}(T_{a0} - t_a)$.

The extension of UPM to the bivariate case is now straightforward. Considering the minimum value T_m within the nominal area A as the second random variable, we need to consider the joint pdf p_{TaTm} of T_a and T_m so that (3) becomes

$$p_R(R)dR = p_{TaTm}(T_a, T_m)dT_adT_m. \tag{10}$$

Since it results that $c(R, T_m) < 0$, we can pose in a way analogous to (7)

$$t_m \equiv T_{m0} - T_m. \tag{11}$$

It worth noting that $c(R, t_m) > 0$ and, coupled with T_{a0}, the threshold value T_{m0} is defined by

$$\int_0^{R_0} p_R(R)dR = \int_{T_{a0}}^{\widetilde{T}_a} \int_{T_{m0}}^{\widetilde{T}_m} p_{TaTm}(T_a, T_m)dT_adT_m. \tag{12}$$

Since again it holds

$$p_{TaTm}(T_a, T_m)dT_adT_m = p_{tatm}(t_a, t_m)dt_adt_m \tag{13}$$

(9) can be generalized to the bivariate or MPM

$$\int_{R_0}^{\hat{R}} p_R(R)dR = P_R(R \le \hat{R})$$

$$= \int_0^{\widetilde{t}_a} \int_0^{\widetilde{t}_m} p_{tatm}(t_a, t_m)dt_adt_m$$

$$= P_{\mathrm{tatm}}(t_a \le \widetilde{t}_a, t_m \le \widetilde{t}_m) \tag{14}$$

where P_{tatm} is the joint cdf of t_a and t_m, $\widetilde{t}_m = T_{m0} - \widetilde{T}_m$. From (12), the retrieval relation $\hat{R} = f_M(\widetilde{T}_a, \widetilde{T}_m)$ can be obtained. The proposed theoretical framework could be easily extended to IR multispectral measurements in order exploit VIS/IR channel combination [36], [37].

Expression (9) can be further transformed by applying the Bayes theorem (e.g., [24]). In fact, the joint pdf can be handled in the following way:

$$p_{tatm}(t_a, t_m) = p_{ta}(t_a)p_{tm}(t_m|t_a) \tag{15}$$

where $p_{tm}(t_m|t_a)$ is the conditional pdf of t_m to t_a. Thus, the Bayesian form of MPM is given by

$$\int_{R_0}^{\hat{R}} p_R(R)dR = \int_0^{\widetilde{t}_a} p_{ta}(t_a) \int_0^{\widetilde{t}_m} p_{tm}(t_m|t_a)dt_m dt_a. \quad (16)$$

The latter Bayesian form can be used to derive some special simplified form of MPM. If t_m is statistically independent (disjoint) of t_a, then $p_{tm}(t_m|t_a) = p_{tm}(t_m)$ and (14) reduced to the disjoint MPM (D-MPM)

$$\int_{R_0}^{\hat{R}} p_R(R)dR = \int_0^{\widetilde{t}_a} p_{ta}(t_a)dt_m \int_0^{\widetilde{t}_m} p_{tm}(t_m)dt_a \quad (17)$$

i.e., to the product of the probabilities of t_a and t_m. Of course, if $\widetilde{t}_m \to \infty$ or, better, $T_{m0} \to \infty$, then D-MPM reduces to UPM due to the normalization to 1 of pdfs.

Another interesting case is the one where the joint pdf of t_a and t_m can be expressed as

$$p_{\text{tatm}}(t_a, t_m) = p_{tm}(t_m)p_{ta}(t_a|t_m) \equiv \delta(t_m - \widetilde{t}_m)p_{ta}(t_a|t_m) \quad (18)$$

where the pdf of t_m is a Dirac function δ, centered in $\widetilde{t}_m$. In this case, (14) reduced to the conditional MPM (C-MPM) given by

$$\int_{R_0}^{\hat{R}} p_R(R)dR = \int_0^{\widetilde{t}_a} p_{ta}(t_a|\widetilde{t}_m)dt_a \quad (19)$$

where the measured value $\widetilde{t}_m$ is the conditional value of t_a probability density.

Some considerations on the numerical implementation of MPM algorithm family can highlight their computation efficiency. Let us refer to the Bayesian form of MPM, given by (16). If pdfs are approximated by corresponding histograms of occurrences, we can estimate pdf of discrete variables R_i, t_{aj}, and t_{mk} by assuming uniform bins

$$p_R(R_i) = \frac{N_{Ri}}{N_S \Delta R_i}$$

$$p_{ta}(t_{a_j}) = \frac{N_{t_{a_j}}}{N_S \Delta t_{ai}}$$

$$p_{tm}(t_{m_k}|t_{a_j}) = \frac{N_{tm_k}|N_{t_{a_j}}}{N_S \Delta t_{mi}} \quad (20)$$

where N_{Ri} and N_S are the number of data in the ith bin R_i and the total number of space–time coupled data (records) in the given subregion S, respectively. Assuming a uniform bin size ΔR, i.e., $\Delta R_i = \Delta R$, the pdf normalization property implies that

$$\sum_{i=1}^{N_R} p_R(R_i)\Delta R_i = \Delta R \sum_{i=1}^{N_R} p_R(R_i) = 1 \quad (21)$$

where N_R are the number of available bins for R such that $N_R = [\max(R) - \min(R)]/\Delta R$. Analogous notations are valid for the discrete variables t_{aj} and t_{mk}. By substituting (20) into (16), we obtain

$$\sum_{i=1}^{N_{\hat{R}}} N_{Ri} = \nu \sum_{j=1}^{N_{\widetilde{t}a}} N_{t_{a_j}} \sum_{k=1}^{N_{\widetilde{t}m}} \left(N_{tm_k}|N_{t_{a_j}}\right) \quad (22)$$

where $\nu = 1/N_S$ and $N_{\hat{R}}$, $N_{\widetilde{t}a}$, $N_{\widetilde{t}m}$ are the number of occurrences relative to the ith, jth, and kth bin, respectively, such that $R_i = \widetilde{R}$ is the estimate, and $t_{aj} = \widetilde{t}_a$, $t_{mk} = \widetilde{t}_m$ are the IR measurements. The last formula suggest an effective numerical implementation of MPM by means of lookup tables. The discretization of involved variables, i.e., R_i, t_{aj} and t_{mk}, can play a role in the accuracy of the inversion algorithm and will be considered in the next sections.

B. VMR

Another classical choice when dealing with the statistical inversion problem in a multivariate context is to resort to the multiple regression method. Again, our goal is to derive the estimate $\hat{R}$ from a set of IR radiometric measurements, i.e., $\widetilde{T}_a$ and $\widetilde{T}_m$, with a given subregion S where N_S are supposed to be available, i.e., to find a relation the inversion relation $\hat{R} = f_R(\widetilde{T}_a, \widetilde{T}_m)$. A matrix formulation of the problem can be useful to introduce the proposed regression technique.

Let us consider a measurement vector $= \widetilde{\mathbf{T}} = [\widetilde{T}_a \ \widetilde{T}_m]'$, where the prime indicates array transposition. If the unknown estimator function $\hat{R} = f_R(\widetilde{\mathbf{T}})$ is expanded in a Taylor series around the mean value $\langle \mathbf{t} \rangle$, a polynomial expression of an arbitrary degree M with unknown expansion coefficients can be written. The polynomial terms can be either powers of $\widetilde{T}_a$ and $\widetilde{T}_m$ or powers of their mixed terms. By neglecting the mixed terms, for simplicity, a generalized predictor vector, characterized by polynomial variables centered around the mean can be introduced, i.e., $\Delta\widetilde{\mathbf{t}} = [\Delta\widetilde{T}_a \ \Delta\widetilde{T}_m \ \Delta\widetilde{T}_a^2 \ \Delta\widetilde{T}_m^2 \ldots \Delta\widetilde{T}_a^M \ \Delta\widetilde{T}_m^M]'$ such that

$$\Delta\widetilde{T}_a \equiv \widetilde{T}_a - \langle\widetilde{T}_a\rangle = \widetilde{T}_a - \frac{1}{N_S}\sum_{s=1}^{N_S}\widetilde{T}_{as}$$

$$\Delta\widetilde{T}_m \equiv \widetilde{T}_m - \langle\widetilde{T}_m\rangle = \widetilde{T}_m - \frac{1}{N_S}\sum_{s=1}^{N_S}\widetilde{T}_{ms}. \quad (23)$$

If a training dataset is available, the search for expansion coefficients can be accomplished by means of an inverse linear problem by minimizing the sum of square errors between the polynomial estimator $\hat{R} = f_R(\widetilde{\mathbf{T}})$ and the known value R. The solution to this problem is called ordinary multiple regression (OMR) and is given by

$$\hat{R} = \langle R \rangle + \mathbf{D}_{\text{OMR}}\Delta\widetilde{\mathbf{t}} = \langle R \rangle + \mathbf{C}_{Rt}\mathbf{C}_t^{-1}\Delta\widetilde{\mathbf{t}} \quad (24)$$

where, consistently with (23), $\langle R \rangle$ is given by

$$\langle R \rangle = \frac{1}{N_S}\sum_{s=1}^{N_S} R_s. \quad (25)$$

In (24), $\mathbf{D}_{\text{OMR}}$ is the OMR coefficient matrix, $\mathbf{C}_{Rt}$ and $\mathbf{C}_t$ are the cross covariance between R and $\Delta\widetilde{\mathbf{t}}$ and the autocovariance of $\Delta\widetilde{\mathbf{t}}$, respectively, whose estimate is given by

$$\mathbf{C}_{Rt} \cong \frac{1}{N_S - 1}\sum_{s=1}^{N_S} R_s\Delta\widetilde{\mathbf{t}}_s'$$

$$\mathbf{C}_t \cong \frac{1}{N_S - 1}\sum_{s=1}^{N_S} \Delta\widetilde{\mathbf{t}}_s\Delta\widetilde{\mathbf{t}}_s'. \quad (26)$$

Note that OMR is sometimes referred to as ordinary least square solution or *D-matrix* technique.

Apart from its implementation simplicity, a further appealing aspect of (24) is that it can be deduced even under particular constraints in order to ensure more robustness to test data noise. This feature is very suitable in our context, since the rainfall R, which we consider to be "true," are indeed derived by MW-based inversion algorithms as expressed by (2). Thus, apart from instrumental noise, a further random error should be taken into account due to the so-called *calibration step*. As already mentioned, MW radiometric estimation of rain over land is one of the major sources of inaccuracy, but space–time undersampling of a given subregion should be considered as well. Thus, the inverse problem can be represented by a random error $\boldsymbol{\varepsilon}_t$, affecting $\Delta\widetilde{\mathbf{t}}$, presenting both a systematic and a random component.

In this scenario, it would be highly recommended to devise an rain estimator $\hat{R} = f_R(\widetilde{\mathbf{T}})$ with a special robustness with respect to these uncertainties [34], [35]. Extending the OMR approach, it is possible to give a robust estimation of R, based on a variance-constrained multiple regression method whose formulation is given by

$$\hat{R} = \langle R \rangle + \mathbf{D}_{\mathrm{VMR}}\Delta\widetilde{\mathbf{t}} = \langle R \rangle + \mathbf{C}_{Rt}\left(\mathbf{C}_t^{-1} + \gamma\mathbf{C}_v\right)\Delta\widetilde{\mathbf{t}} \quad (27)$$

where $\mathbf{D}_{\mathrm{VMR}}$ is the VMR coefficient matrix, γ is the *constraint factor*, and $\mathbf{C}_v$ is a diagonal matrix derived from the autocovariance matrix $\mathbf{C}_t$. Details on the derivation of (27) are exposed in [36]. Notice that for $\gamma = 0$ (27) yields (24), while by definition $\gamma = 1$ means to double the variances of $\mathbf{C}_t$.

The critical aspect in the use of (27) is the choice of the constraint γ. Empirical ways can be followed by successive trials starting. An objective criterion is to ensure that the estimates $\hat{R}$ must be positive defined for any $\Delta\mathbf{t}$ belonging to the training dataset, starting from $\gamma = 0$. This physical condition can be formulated as

$$\gamma : \hat{R} = \langle R \rangle + \mathbf{C}_{Rt}(\mathbf{C}_t + \gamma\mathbf{C}_v)^{-1}\Delta\widetilde{\mathbf{t}} \geq 0 \quad \forall\Delta\widetilde{\mathbf{t}}. \quad (28)$$

If (24) already satisfies the previous condition, γ is obviously set to zero.

An interpretation of (27) can be given in terms of singular value decomposition (SVD) analysis of $\mathbf{C}_t$. When SVD is applied to a symmetric (covariance) matrix, it reduces to principal component analysis (PCA), which can be stated in terms of the ith eigenvector $\mathbf{a}_{ti}$ and associated eigenvalues λ_i of the following eigenvalue problem:

$$(\mathbf{C}_t - \lambda_i\mathbf{I})\mathbf{a}_{ti} = 0 \quad (29)$$

where $\mathbf{I}$ is the identity matrix. Each eigenvalue λ_i is proportional to the variance of the corresponding principal component with the well-known normalization property

$$\sum_{i=1}^{M}\lambda_i = 1 \quad (30)$$

being λ_1 and λ_M the largest and the smallest eigenvalue, respectively. Assuming an equal noise level for each channel, if $\sigma_{\varepsilon t}^2$ indicates the variance of the random error $\boldsymbol{\varepsilon}_t$, then the SNR can be defined as

$$\mathrm{SNR} = \frac{\lambda_M^2}{\sigma_{\varepsilon t}^2}. \quad (31)$$

By applying SVD to the constrained covariance $(\mathbf{C}_t + \gamma\mathbf{C}_v)$, due to its structure it can be shown that this covariance has the smallest eigenvalues λ_{cM} always larger than λ_M (if $\gamma \neq 0$). It results that

$$\lambda_{cM} = \lambda_M + \gamma C_{vMM} \quad (32)$$

where C_{vMM} is the Mth diagonal element of $\mathbf{C}_v$. This implies that, given the same noise level, VMR is implicitly increasing SNR with respect to OMR. The price of a robust inversion is related to a smoothness of the retrieval solution, which converts into a slightly less accuracy of the rain estimates when data are not affected by anomalous conditions.

Finally, by using (26) together with (27), we can write a polynomial VMR estimator of R as

$$\hat{R} = d_0 + \sum_{m=1}^{M} d_{1m}(\widetilde{T}_a)^m + d_{2m}(\widetilde{T}_m)^m \quad (33)$$

where d_0, d_{1m}, and d_{2m} are the regression coefficients.

C. Literature Algorithms

Satellite-based rain algorithms, using the probability matching technique, have been already developed by several authors [19]–[21]. The approach is basically similar to what we have called univariate probability matching and whose formulation is given by (6). Some differences may arise with respect to: 1) the choice of the minimum rain-rate threshold R_0; 2) the discretization of the histogram bins; 3) the dimension of subregions. Besides, instead of using the matching of pdf as in (6), some authors prefer to match the first of higher statistical moments of both random variables. Since these differences are conceptually minor ones, we used UPM as a reference in this by applying the same implementation choices considered for the MPM technique.

The regression method has been also used in literature [18], [21]. An example is the so-named microwave-infrared rain retrieval algorithm (MIRRA) [21]. This is basically similar to the one here described. A cutoff minimum IR brightness temperature T_{mc} is chosen to separate the data into raining (i.e., $T_{\mathrm{IR}} \leq T_{mc}$) and nonraining (i.e., $T_{\mathrm{IR}} > T_{mc}$) subgroups and calculated in the considered subregion as follows:

$$T_{mc} = \mu_r + N_R\frac{\mu_n - \mu_r}{N_N + N_R} \quad (34)$$

where μ_r and μ_n are the mean T_m for the raining and nonraining subgroups of data pairs, respectively, and N_R and N_N represent the number of raining and nonraining pairs in each subgroup. Once T_{mc} has been found, a regression line is anchored at the point $R = 0$ and $\widetilde{T}_m = T_{mc}$ in the $R - \widetilde{T}_m$ plane. Considering only the raining data subgroup, an ordinary least square technique is used to derive the rain-rate estimate by means of

$$\hat{R} = a + b\widetilde{T}_m \quad (35)$$

where a and b are regression coefficients. The update of the latter coefficients is performed whenever a new set of LEO–MW data are available. A minimum of at least ten coincident LEO–MW-derived rain rates higher than a threshold of 1 mm/h are requested.

Apart from (34), the MIRRA method, tested on the tropical data, is analogous to the VMR technique, illustrated in Sec-

tion II-B, with the constraint factor equal to zero, a choice of a first-order polynomial ($M = 1$) and a use of only T_m data. MIRRA will be used as a comparison algorithm in the next sections by using as a training set the combined data in the given subregion.

III. DATA ANALYSIS

In this section, some details about the MICRA preprocessing step will be given together with the definition of the score indexes to be used in the data analysis.

A. Data Preprocessing

MICRA statistical integration techniques, described in Section II, can be applied to combined MW–IR data in a given subregion S to derive the R–T_{IR} inverse relationship. The behavior of such algorithms is expected to be affected by surface conditions and rain regimes. The evolution of precipitation systems is strongly dependent on whether the embedded environment is maritime or continental [40]. On the other hand, rain structure can differ a lot if the regime is basically stratiform or convective giving rise to moderate or intense precipitation [5], [7].

A way to maintain a sort of "homogeneity" within the training combined dataset with respect to these feature is to *preclassify* combined data within each nominal area A and then apply the foreground process to each class separately. This approach has the advantage to introduce a physical point of view within the construction of the training dataset and can be equivalent to perform a stepwise statistical inversion. On the other hand, it can limit the number of available realizations within each class and can bring a further misclassification component within the total error budget.

A simple approach to subregion classification is to defined five precipitation classes as follows:

1) moderate (stratiform) rain over land;
2) intense (convective) rain over land;
3) moderate (stratiform) rain over ocean;
4) intense (convective) rain over ocean;
5) rain over coastlines.

The identification of surface type is provided by satellite navigation data whose accuracy can be estimated to be about a pixel or a fraction of pixel. Coastline identification at the MW sensor spatial scale (order of tens of kilometers) reveal to be highly affected by geolocation errors and by mixed surface emissivity conditions [33]. The latter error source can be quite significant if MW lower frequency are predominantly used. From this perspective, the introduction of the last class (rain over coastline) is aimed to enucleate this problem.

A more complicated issue is the classification of rain regimes. Indeed, this label could be provided by the passive MW retrieval algorithm, given in (1). This feature can be extracted both from empirical and from model-based techniques, while MW operational algorithms do not generally attempt to provide this information [5], [30], [39]. IR observations can also be used to identify rain regimes, especially the convective ones, even though some ambiguities with respect to cirrus clouds must be solved [18], [36], [40]. In the following steps, we assume that

the surface identification has been already carried out so that rain regime is separately identified over land and ocean.

In case of unavailability of cloud classification label, the simplest approach is to use a rain-rate threshold R_t and to identify a moderate (stratiform) regime when $R \leq R_t$ and an intense (convective) regime when the opposite occur. Values for R_t can range from 5–15 mm/h, considering that R is a product at a fairly low spatial resolution when estimated from satellite MW radiometers.

As an alternative, a threshold approach can be applied to IR measurements instead of R estimates. Generally speaking, higher T_{IR} are associated to lower clouds with stratiform rainfall, while lower T_{IR} are attributed to tall cumuliform clouds with intense precipitation. When coupling MW and IR data, the ambiguity due to cirrus clouds is automatically removed being MW sensing not affected by ice clouds. In order to be less dependent on meteorological conditions, a simple classification of "high" raining clouds can be performed by discriminating with respect to the differential temperature t_a, defined in (7), by means of the following criterion:

$$\widetilde{t}_a = (T_{a0} - \widetilde{T}_a) < t_{at} \tag{36}$$

where t_{at} is the threshold value. The latter can assume values between 40 and 50 K. "Low" raining clouds are identified when (36) is not satisfied.

An third choice is to performed a unsupervised classification to derive centroids $m_R^{(k)}$ and variances $\sigma_R^{2(k)}$ (with respect to the centroids) of moderate ($k = 1$) and intense ($k = 2$) rain classes by using an historical archive for each subregion S. Then, a maximum-likelihood (ML) classification technique can be applied by minimizing the following objective function:

$$d_{ML}(k, R) = \frac{\left(R - m_R^{(k)}\right)^2}{\sigma_R^{2(k)}} \tag{37}$$

where a Gaussian pdf for R deviations has been assumed.

As already mentioned, the validation of the two integration techniques has been carried out considering only nearly coincident MW and IR passages over a given classified subregion S. The maximum delay between IR and MW available images is at most equal to the half of GEO sensor recording period (e.g., about 15 min for Meteosat VISSR). Once a new, coincident MW and IR passage occurs, an automated task is started to process the available statistic files, sorted by time, using the geolocation data for each collocated data point to build up separate datasets of IR temperatures and associated MW rain rates for the appropriate box.

To assure that only the most recent rain history is captured, the rain rates R and the IR temperatures T_{IR} datasets are filled until the data occurrence within a given subregion exceeds a threshold. This *occurrence threshold* N_{St} expresses the number of pixels, covered by MW–IR combined data, to which MPM and VMR are then applied. A criterion to established this occurrence threshold can be linked to the bin resolution of data histograms in the sense that, if N_b is the number of bins through which a pdf is approximated, then

$$N_{St} \cong \rho N_b \tag{38}$$

	Observed Rain	**Observed No-Rain**
Detected Rain	$n_{R\hat{R}}$	$n_{N\hat{R}}$
Detected No-Rain	$n_{R\hat{N}}$	$n_{N\hat{N}}$

where ρ is multiplicative factor. Note that N_b represent the number of rain-rate bins N_R and temperature bins N_T, as in (22). For a statistical significance of the dataset, a rule of thumb is to set α between 4 and 7, while N_b can range from 100–150. Depending upon how recently a given geographical region was scanned by a LEO–MW, the overall data used in some of the subregion datasets may be only a few hours old, whereas other regions may require a longer "memory" time to reach the coverage threshold, that is $N_S > N_{St}$. A maximum lookback time limit of 24 h is generally set. If a subregion has not reached the coverage threshold by this time, this region is marked as "*unavailable*," until eventually an update cycle will capture newly observed microwave data in this subregion.

As a last step of the preprocessing stage, a percentage ratio P_{NR}, expressing the number of the nonraining combined data N_N with respect to all combined data N_S within each subregion, has been introduced, i.e.,

$$P_{NR} = 100 \frac{N_N}{N_S} = 100 \frac{N_N}{N_N + N_R} \qquad (39)$$

where N_R are the raining data. If a threshold P_{NRt} is exceeded in a given subregion, the retrieval phase is forced to assign a zero R value to each pixel in that subregion. Values of P_{NRt} can range from 90% to 99%.

B. Analysis Indexes

In order to systematically analyze the results, we have introduce a fairly large set of indexes to quantify both the detection and estimation accuracy of the considered rainfall combined algorithms.

The first set of six indexes allows to evaluate the rain detection capability of each method, i.e., to discriminate between raining and nonraining pixels. Table I illustrates the so-called *contingency table*, which provides the number of correctly and incorrectly classified pixels with respect to rain and no-rain regimes. Nomenclature is such that the "observed" (true) pixels are those whose rain is derived from MW-LEO sensors, while the "detected" ones are those whose rain is derived from IR-GEO integration technique at the same collocated time. A threshold value of 0,1 mm/h for rainfall is selected to delineate rain areas both for observed and detected rain-rate values. Moreover, the first subscript of n in the table stands for the observed pixel, while the second for the detected one. Thus, $n_{R\hat{R}}$ and $n_{R\hat{N}}$ express the number of pixels, detected as rain and no-rain, respectively, when the observed pixel is a rain one. On the opposite, $n_{N\hat{R}}$ and $n_{N\hat{N}}$ expresses the number of pixels, detected as rain and no-rain, respectively, when the observed pixel is a no-rain one. It is clear, from these definitions, that $n_{R\hat{R}}$ and $n_{N\hat{N}}$ are the number of correctly classified pixels, while both $n_{R\hat{N}}$ and $n_{N\hat{R}}$ indicate erroneous detection.

From the contingency table, it is straightforward to introduce some useful score indexes, able to highlight specific capabilities of the detection algorithms. These indexes are defined in Table II where the worst and best values are also indicated for clarity. The probability of detection of rain (PODR) and the false-alarm ratio (FAR) have to be considered together because, for instance, the extreme case to detect precipitation everywhere would result in a high PODR, but in a large FAR as well. The same is true for the PODR and the probability of detection of rain (PODNR) because, in case of estimating precipitation everywhere, would result in a high PODR, but also in a low PODNR. The critical success index (CSI) is a severe score because it gives no credit for the correct identification of no-rain pixels, which are generally the majority with a subregion. The Hansen and Kuiper index (HKI) accounts properly for both rain and no-rain pixels. Relevance of over- and underestimation effects is measured by the index of symmetry error (ISE): an unbiased estimate scores a zero value of ISE, while ISE takes negative (positive) values in case of overestimation (underestimation).

The second set of parameters, reported in Table III, allows to evaluate the rain estimation capability of each combined method. In Table II, where the worst and best values of each parameter are also indicated, N_T is the total number of combined MW–IR observations, available in all subregion along the test period, while ε_R is the rain-rate error between observed R and estimated $\hat{R}$ values, i.e.,

$$\varepsilon_R = \hat{R} - R. \qquad (40)$$

Thus, $\overline{R}$ represents the mean value of MW-based rain rates, $\overline{\varepsilon}_R$ the mean value (bias) of the rain-rate estimate errors, while σ_R^2 and $\sigma_{\varepsilon_R}^2$ are the standard deviations of rain rates and rain-rate estimate errors, respectively. Note that, while the normalized error bias (NEB) and the fractional mean reduction (FMR) are measures of the error bias or mean value, the fractional variance reduction (FVR) and fractional standard error (FSE) are a measure of the error variance and root mean square value, respectively.

IV. APPLICATION

Two case studies have been utilized to evaluate the MICRA statistical integration techniques. Satellite data have been collected from SSM/I aboard DMSP platforms, from TMI aboard TRMM and from VISSR aboard MeteoSat platforms. The background and foreground processes have been run for each case study, and various integration techniques, such as UPM, MPM, VMR, and MIRRA, have been intercompared in terms of both detection and estimation accuracy.

A. Sensitivity Analysis

As already mentioned, starting from IR temperatures within each subregion and with a 24-h backward window, we have estimated the rain rate using both MPM and VMR methods. This rain-rate estimate has been then compared with the MW-derived rain rates, available from the subsequent LEO–MW sensor overpass and used as a reference ("ground truth"). This evaluation strategy has been set up basically to assess the capability of each integration technique to "calibrate" IR measurements in terms of rain rate.

TABLE II
RAIN DETECTION INDEXES, USED TO EVALUATE THE RAIN DETECTION CAPABILITY OF EACH METHOD, I.E., TO DISCRIMINATE BETWEEN THE RAINING AND
NONRAINING PIXELS. FOR EVERY INDEX IT IS ALSO REPORTED ITS WORST AND BEST VALUE

Analysis Index	Expression	Worst value	Best Value
PODNR (Probability Of Detection of No Rain)	$\dfrac{n_{N\hat{N}}}{n_{N\hat{R}} + n_{N\hat{N}}}$	0	1
PODR (Probability Of Detection of Rain	$\dfrac{n_{R\hat{R}}}{n_{R\hat{N}} + n_{R\hat{R}}}$	0	1
FAR (False Alarm Ratio)	$\dfrac{n_{N\hat{R}}}{n_{R\hat{R}} + n_{N\hat{R}}}$	1	0
HKI (Hansen and Kuiper Index)	$\dfrac{n_{R\hat{R}}}{n_{R\hat{R}} + n_{N\hat{R}}} - \dfrac{n_{N\hat{R}}}{n_{N\hat{R}} + n_{N\hat{N}}}$	-1	1
CSI (Critical Success Index)	$\dfrac{n_{N\hat{N}} - n_{N\hat{R}}}{n_{R\hat{N}} - n_{N\hat{R}}}$	0	1
ISE (Index of Symmetry of Error)	$\dfrac{n_{R\hat{R}}}{n_{R\hat{R}} + n_{R\hat{N}} + n_{N\hat{R}}}$	±1	0

TABLE III
RAIN ESTIMATION INDEXES, USED TO EVALUATE THE RAIN ESTIMATION CAPABILITY OF EACH METHOD, I.E., TO COMPUTE THE ACCURACY OF RAINFALL RATE
RETRIEVAL FOR A GIVEN PIXEL. FOR EVERY INDEX IT IS ALSO REPORTED ITS WORST AND BEST VALUE

Analysis Index	Expression	Worst value	Best Value
NEB (Normalized Error Bias)	$\dfrac{\dfrac{1}{N_T}\sum\limits_{i=1}^{N_T} \varepsilon_{R_i}}{\dfrac{1}{N_T}\sum\limits_{i=1}^{N_T} R_i} = \dfrac{\overline{\varepsilon}_R}{\overline{R}}$	∞	0
FMR (Fractional Mean Reduction)	$\dfrac{\overline{R} - \overline{\varepsilon}_R}{\overline{R}}$	$-\infty$	1
FVR (Fractional Variance Reduction)	$\dfrac{\sigma_R^2 - \sigma_{\varepsilon_R}^2}{\sigma_R^2}$	$-\infty$	1
FSE (Fractional Standard Error)	$\dfrac{\sqrt{\overline{\varepsilon}_R^2 + \sigma_{\varepsilon_R}^2}}{\overline{R}}$	∞	0

Before intercomparing the various MICRA algorithms, a sensitivity study has been accomplished to determine the most critical configuration parameters. This sensitivity analysis has been carried out by using a large historical combined test dataset, spanning over one year (from November 1999 until November 2000) and not containing the two case studies presented here. As mentioned before, for simplicity we restricted our analysis to data coming from DMSP, TRMM, and Meteosat satellites.

The first parameter we have considered is the dimension and the spacing of the subregions S in which the entire region of interest is divided. This has been accomplished by subdividing the entire region of interest into smaller partially overlapping, subregions. Starting from $\alpha = 15°$ and $\beta = 5°$, an optimal value, intended as the value that compromises at best retrieval accuracy and computation efficiency, it has been found $\alpha =$ $9°$ and $\beta = 3°$, where α is the subregion dimension, while β represents the spacing.

As second step, we have considered the maximum temporal look-back within the background process. We found that a look-back of 24 h can be considered a good compromise between the need of accumulating a consistent number of pixels to derive the R–T_a relationship and the need to have data as close as possible in time to the storm evolution on that subregion.

A suitable discretization of the histograms to implement pdfs has been also considered. Starting from 1 mm/h and 1.5 K, the found optimal values have been a constant bin of 0.25 mm/h for RR histograms and a constant bin of 1 K for T_{IR} histograms. Moreover, the multiplicative factor ρ in (38) has been set to 5, while the number of bins to 120 so that the subregion number

TABLE IV
RESULTS IN TERMS OF ANALYSIS INDEXES, DEFINED IN TABLES II AND III, AS OBTAINED FROM THE SENSITIVITY ANALYSIS OF THE MPM. THE COMPARISON OF THE MPM INITIAL VERSION WITH THE OPTIMAL ONE AND THE UPM IS ALSO SHOWN. IDEAL VALUES OF THE INDEXES ARE REPORTED FOR CONVENIENCE

Analysis Index	UPM	Initial MPM	Optimized MPM	Ideal value
PODNR	0,96	0,97	0,98	1
PODR	0,34	0,36	0,35	1
FAR	0,63	0,59	0,56	0
CSI	0,23	0,24	0,25	1
HKI	0,34	0,38	0,45	1
ISE	0,10	0,09	0,06	0
NEB	0,08	0,07	0,06	0
FMR	0,92	0,93	0,94	1
FVR	0,91	0,91	0,93	1
FSE	0,61	0,57	0,55	0

TABLE V
SAME AS FOR TABLE IV, BUT FOR THE VMR METHOD. RESULTS FOR FIRST-ORDER OMR ARE ALSO SHOWN

Analysis Index	First-order OMR	Initial Cubic-order VMR	Optimized Cubic-order VMR	Ideal value
PODNR	0,63	0,66	0,68	1
PODR	0,84	0,91	0,92	1
FAR	0,87	0,86	0,75	0
CSI	0,13	0,14	0,22	1
HKI	-0,24	-0,21	0,14	1
ISE	-0,98	-0,93	-0,70	0
NEB	0,08	0,08	0,06	0
FMR	0,91	0,92	0,94	1
FVR	0,94	0,95	0,96	1
FSE	0,55	0,47	0,45	0

threshold N_{St} has been assumed to be 600 (effective values between 500 and 1000 are acceptable). Starting from 99%, we have also searched for an optimum value of no-rain pixel threshold P_{NRt}, found equal to 95% [see (39)]

As far as MPM is concerned, we have set the threshold rain-rate R_0 [see (5) and (12)] to 0.1 mm/h, while the range of IR temperature to be spanned has been fixed between 173 and 293 K. It is worth mentioning that the results obtained for MPM are generally slightly better than the disjoint MPM (D-MPM) and conditional MPM (C-MPM), given in (17) and (19), respectively. This is the reason why we show, for brevity, only results for MPM even though D-MPM and C-MPM can represent a valid alternative especially in terms of computation efficiency.

For the VMR integration algorithm, a natural step was the investigation of the best polynomial order in (33). The choice of a third-order polynomial (i.e., $M = 3$) has been assessed by considering both the retrieval accuracy and computation performances. By introducing the T_{IR} standard deviation σ_T [see (1)] within the predictor set, a further improvement has been verified so that the VMR prediction algorithm, given in (33), has been extended as

$$\hat{R} = d_0 + \sum_{m=1}^{M} d_{1m}(\widetilde{T}_a)^m + d_{2m}(\widetilde{T}_m)^m + d_{3m}(\sigma_{\widetilde{T}})^m \quad (41)$$

where d_0, d_{1m}, d_{2m}, and d_{3m} are the regression coefficients. It is worth mentioning the inclusion of σ_T within the MPM method did not produce significant improvements, while heavily affecting the computation efficiency.

A final study has been carried out on the choice of the pre-classification techniques, illustrated in Section III-A. Again, in order to balance accuracy and efficiency, the optimal choice has resulted to be the simple technique, expressed by (36), after selecting the surface background (land, ocean, or coast). The mean value of the threshold t_{at} has been found to be about 45 K with a standard deviation of 4 K.

In summary, by using the historical test dataset, the comparison between the MICRA prediction algorithms with the initial and optimized configuration parameters are shown in Table IV
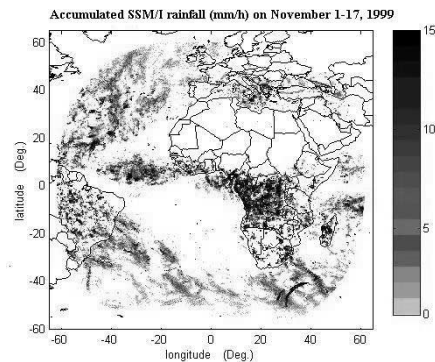

Fig. 2. Accumulated rainfall (millimeters per hour), derived from LEO–MW radiometers, during November 1–17, 1999 (November 1999 case study).

for MPM and in Table V for VMR in terms of a variety of analysis indexes, defined in Tables II and III. For convenience, ideal values of each index are reported. Univariate PM and first-order polynomial OMR algorithms are also listed for comparison in Tables IV and V, respectively. Both UPM and first-order OMR give overall worse results than MPM and cubic-order VMR. By substituting the default values with the optimum values, the improvement of MPM algorithm performances in terms of retrieval accuracy ranges from 5% to 15% for the optimized MPM with respect to initial MPM (with respect to UPM the improvements are higher than 20%) without degrading their computation performances. For the optimized VMR, the improvements with respect to its initial configuration are even higher going from 5% to 30% (up to 50% if compared with first-order OMR).

B. Case Studies

The first case study refers to the period November 1–17, 1999 (hereafter referred to as *November 1999* case). Heavy rainfall occurred on the Atlantic area and along the equator, as seen from Fig. 2, where the total accumulated rainfall, as estimated from LEO–MW sensors, is plotted. Consider an effect of possible undersampling of a rainfall event due to the LEO platform observations. During this period, strong cyclonic perturbations hit the Mediterranean area. The period from November 7–11 coincided with the eleventh intensive operational period (IOP-11) of the
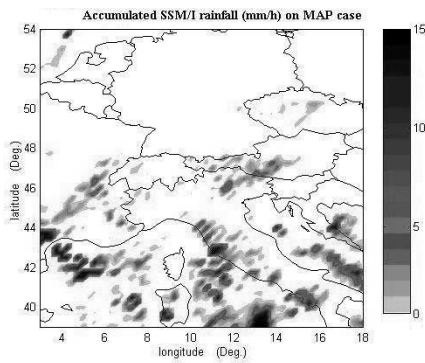
Fig. 3. Same as in Fig. 2, but for the Southern Europe zoomed area. Northern Italy and southern Switzerland and Austria were interested by the Mesoscale Alpine Project during the considered period.
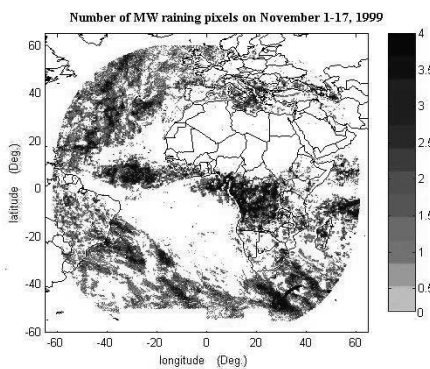

Fig. 4. Number of collocated MW–IR radiometric measurements relative to rain pixels, available during November 1–17, 1999 (November 1999 case study).

Fig. 5. Same as in Fig. 2, but for the period November 16–27, 2000 (November 2000 case study).
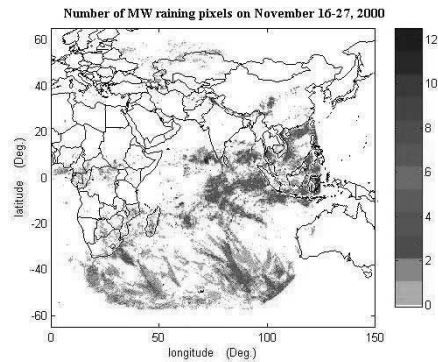
Fig. 6. Same as in Fig. 4, but for the period November 16–27, 2000 (November 2000 case study).

Mesoscale Alpine Project (MAP), which was carried out in a vast region delimited by northern Italy and southern Switzerland and Austria. To this aim, Fig. 3 shows a zoom of Fig. 2 on the Southern Europe regions.

In order to apply, the combined MW–IR dataset has to be built. Fig. 4 shows the number of collocated MW–IR raining measurements per pixel available within the November 1999 case. Note that subregions are made by about $10° \times 10°$ boxes so that they can contain more than 1600 pixels.

The second case study refers to the period November 16–27, 2000 (hereafter referred to as November 2000 case). In this case, the integration techniques have been evaluated on a global scale, including the whole field of view of METEOSAT-5. During this second case study, light but persistent rainfall occurred on the Indian Ocean and on the southeast of Asia. Fig. 5 shows the same as in Fig. 2, but for the November 2000 case, while Fig. 6 is analogous to Fig. 4.

It is worth mentioning to note that the two case studies have shown some peculiar differences with respect to combined IR temperature pdfs in case of rain and no-rain, mainly depending on rain climatology. These differences can be appreciated from Figs. 7 and 8, where the IR temperature histograms are reported for no-rain and rain pixels, respectively, for both the November 1999 and November 2000 case studies.

For no-rain pixels, the IR temperature distributions of the two cases are quite similar, showing a tail for T_a less than 250 K, which is the major cause of erroneous detection of rainfall.
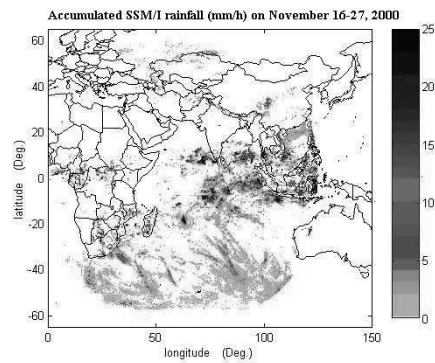
When considering rain pixels in Fig. 8, the pdf appearance is strongly different for the two cases. While the November 1999 case is characterized by a significant uniform spread for lower and higher IR temperatures (with values down to 200 K), the T_a distribution for the November 2000 case is mainly concentrated for T_a larger than 250 K. This results seem to be an indication, on one hand, of the presence of high convective clouds (with top height as high as 10 km) within the November 1999 case, on the other hand of heavy shallow clouds in the November 2000 case.

Indeed, from Figs. 2 and 4, we noted that the rainfall of November 1999 case has large portions over land over Africa and Southern Europe, while the November 2000 is basically characterized by rain over the Indian ocean. As confirmation, Figs. 9 and 10 show the IR temperature and rain-rate pdfs, respectively, for rain pixels over ocean and over land for November 1999 case (see Fig. 2). From a probabilistic point of view, continental and maritime regimes seems to have a very unique signature [38]. This result has been confirmed by other analyses as well we carried out, even though is shows a regional dependence. The same analysis, carried out for the November 2000 data, seems not to be as clear as for the November 1999 data. As discussed later, we may attribute this different behavior to the predominance of shallow clouds over the Indian ocean background within the November 2000 data.

The overall results in terms of previously mentioned indexes are reported in Table VI for the November 1999 and November 2000 cases for the MPM, VMR, UPM, and MIRRA techniques.
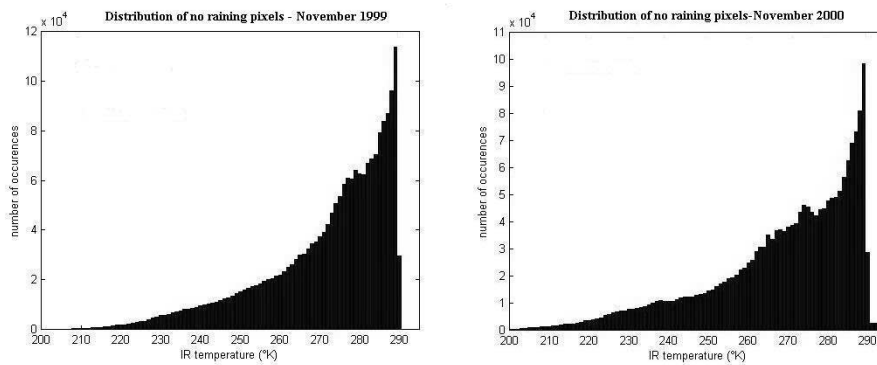
Fig. 7.   Histogram of IR average temperatures relative to the no-rain pixels for the November 1999 and November 2000 case studies.
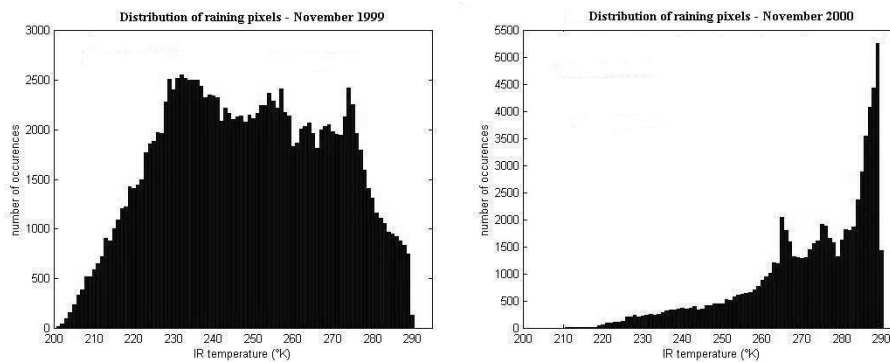

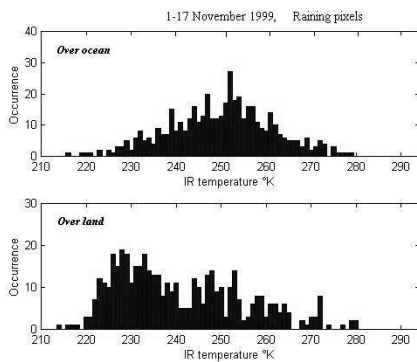Fig. 8.   Same as in Fig. 6, but for the rain pixels.

Fig. 9.   Histogram of IR average temperatures relative to the rain pixels for the November 1999 case (top) over ocean and (bottom) over land. Mean IR temperature is 249.9 K over ocean and 240.8 K over land.
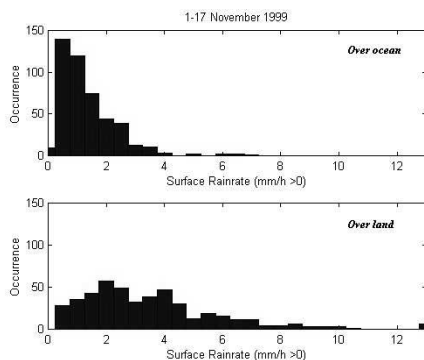

Fig. 10.   Same as Fig. 9, but for MW-derived rain rates (R). Mean rain rate is 1.5 mm/h over ocean and 3.8 mm/h over land.

TABLE VI
RESULTS FOR THE NOVEMBER 1999 AND NOVEMBER 2000 CASES, GIVEN IN TERMS OF ANALYSIS INDEXES, DEFINED IN TABLES II AND III, FOR THE MPM, VMR, UPM, AND MIRRA, AVAILABLE IN THE LITERATURE

Index	Nov. 1999 case				Nov. 2000 case			
	MPM	VMR	UPM	MIRRA	MPM	VMR	UPM	MIRRA
PODNR	0,96	0,71	0,96	0,92	0,98	0,73	0,97	0,95
PODR	0,37	0,51	0,15	0,35	0,12	0,75	0,04	0,13
FAR	0,63	0,88	0,64	0,86	0,86	0,90	0,89	0,89
CSI	0,22	0,11	0,12	0,10	0,07	0,10	0,03	0,04
HKI	0,32	-0,17	0,33	0,12	0,11	-0,16	0,09	-0,01
ISE	0,01	-0,77	0,49	-0,15	0,07	-0,93	0,44	0,04
NEB	0,10	0,12	0,11	0,12	0,14	0,07	0,14	0,12
FMR	0,89	0,88	0,89	0,89	0,86	0,92	0,86	0,84
FVR	0,84	0,86	0,82	0,86	0,85	0,91	0,84	0,86
FSE	0,77	0,7	0,80	0,71	0,78	0,59	0,79	0,8

For the Southern Europe area during the MAP campaign, results are given in Table VII.

From the analysis of the previous tables, a different behavior emerges when considering the November 1999 and November 2000. For the November 1999 case, MPM shows a PODNR and a FAR better than those of VMR, but at the same time, a worse PODR. The latter is significantly better for VMR with respect to the other techniques for the November 2000. The PODR of MPM is low but better than UPM, while MIRRA technique shows performances comparable to those of MPM, apart from FAR. An interesting feature of MPM is the relatively good values of CSI, HKI, and ISE indexes, indicating a better capability of detecting rain pixels and a basically unbiased behavior of the estimates.

TABLE VII
SAME AS IN TABLE VI, BUT FOR NOVEMBER 1999, LIMITED TO THE
MAP GEOGRAPHICAL AREA OVER LAND

Index	MPM	VMR	UPM	MIRRA
PODNR	0,97	0,74	0,97	0,96
PODR	0,31	0,45	0,18	0,3
FAR	0,70	0,94	0,66	0,88
CSI	0,18	0,05	0,11	0,05
HKI	0,27	-0,2	0,26	-0,30
ISE	-0,04	-0,86	0,51	-0,10
NEB	0,06	0,05	0,11	0,06
FMR	0,94	0,94	0,88	0,93
FVR	0,94	0,92	0,83	0,93
FSE	0,49	0,53	0,79	0,52

If the estimation accuracy indexes are considered, the overall better performances are those of VMR with respect to the other techniques. The MPM method shows a slight improvement with respect to UPM and MIRRA, showing a lower error bias (i.e., low NEB and FMR) for the November 1999 case. The estimate error variance, on the contrary, is minimized when considering the VMR approach, which results to be of particular interest for the November 2000 where all estimation indexes are in favor to VMR.

The latter scenario may be explained by considering some features of the two considered cases. While the November 1999 case is highly characterized by a histogram dispersion of IR temperatures and, thus, high rain-rate values (see Figs. 7 and 8), the November 2000 case is less disperse in terms of IR temperatures. This implies that, for each subregion, the VMR least squared fit needs to follow highly nonlinear relationships.

In summary, VMR demonstrates a better capability to detect the rain pixels with respect to MPM (i.e., high PODR). Both proposed techniques show a very good capability to detect the no-rain pixel, even though VMR shows a tendency to overestimate the number of the rain points. This limitation of the VMR method may be mainly related to the choice of an analytical fitting model, which tend to show a bias for near-zero rain rate values. On the other hand, MPM technique deals with numerical histograms and the no-rain detection is limited only by choice of the near-zero rain bin [see (5) and (12)]. With regard to the estimate accuracy, the two techniques show comparable results in the November 1999 case, which are in turn similar to MIRRA and UPM techniques. On the contrary, in the November 2000 case, VMR shows a better estimate accuracy with respect to the MPM mainly as a consequence of the large difference between the two techniques in the capability of collecting the rain pixels.

Regarding the reliability of the two MICRA algorithms from the analyzed case studies MPM has shown to be more accurate in following variable conditions characterized by high values of rain rates, while the VMR, because of its structure, showed some difficulties when the conditions change in a sudden way or in presence of a high range of rain rates. It is worth noting finally that VMR has showed a better computation efficiency with respect to MPM because of the short time necessary for the computation of the regression coefficients with respect to the time necessary for matching the rain-rate histogram with the IR temperatures histogram.

V. SUMMARY AND CONCLUSION

A systematic analysis of statistical integration methods has been carried out in order to use MW-based rain-rate estimates to "calibrate" IR measurements. The MW–IR combined rainfall algorithm (MICRA) procedure is based on the collocation of GEO–IR and LEO–MW data, accomplished on a global scale using an ensemble of subregions, partially overlapped. Two new techniques, named multivariate probability matching and variance-constrained multiple regression have been investigated in terms of relative estimate accuracy, algorithm parameter sensitivity, cloud classification impact, and computing efficiency. As an application, two case studies have been discussed, in order to demonstrate the potentiality of monitoring rainfall attenuation and precipitation using the proposed MICRA techniques.

Focusing on the MICRA *integration* step as described in Section II, we have shown that the MPM method shows better performances for rain detection and slight lower scores for rain estimation, while the opposite holds for the VMR technique. In many respects, both MPM and VMR show better results than univariate probability matching and linear regression methods. Even though we limited our analysis to DMSP-SSM/I, TRMM-TMI, and MeteoSat-VISSR data, the proposed techniques can be easily generalized to rain-rate estimates, derived from other spaceborne sensors and ground-based instruments, as well as to multispectral VIS/IR channels. We note that the MICRA statistical integration techniques can offer some advantages with respect to artificial neural network approaches due to their higher efficiency within the training phase, which is essential when designing an adaptive rapid-updating procedure on a global scale.

It is worth recalling that the emphasis of our intercomparisons has been put not on the rain-rate estimate validation, but on the testing and verification of MW and IR data fusion techniques to reproduce MW-derived rain-rate fields, assumed as reference data. This approach has highlighted the substantial aspect of a synergetic retrieval based on sensor combination. The validation of the product of the MICRA technique is, in its current form, related to the accuracy of inversion step procedure where surface rain rate is estimated from MW radiometric measurements. Any improvement in the MW-based retrieval technique should reflect into the combined algorithm approach. In this way we have also avoided to tackle the critical problem of comparing ground-based rain-rate measurements with satellite-based ones.

Future work will be devoted to embed these MICRA statistical techniques within current operational frameworks in order to verify the expected improvements and validate them on a long-term and global scale basis by comparing with conventional ground data. Besides, the MW *inversion* step can be refined by using climatologically tuned empirical algorithms and, for some critical regions, physically based MW algorithm able to predict the precipitation spatial structure. Indeed, further retrieval constraints, derived from available geophysical fields (such local wind flow and orography) and meteorological dynamical condition (such as rain cloud advection), can help to improve the estimate of surface rainrate (e.g., [18] and [19]).

The scenario of MW radiometers aboard a multisatellite constellation raises the issue about the consistency of rain-rate prod-

ucts derived from instruments with different specifications (e.g., channel frequencies, field of views, radiometric accuracies). A simple way to apply the proposed MICRA technique could be the choice of a "reference" radiometer whose rain products can be used to "calibrate" all the others [41]. For instance, if TMI is chosen as a "reference" in the tropical regions due to its characteristics and revisit time, then histograms of rain rates derived from other sensor such as SSM/I, AMSU, and AMSR could be adjusted to those of TMI adopting the same probability matching concepts illustrated here. Finally, the recent launch of MeteoSat Second Generation constitutes a unique opportunity to exploit multivariate (multispectral) approaches to satellite rainfall retrieval.

REFERENCES

[1] E. A. Smith, J. Lamm, R. Adler, J. Alihouse, K. Aonashi, E. Barrett, P. Bauer, W. Berg, A. Chang, R. Ferraro, J. Ferriday, S. Goodman, N. Grody, C. Kidd, C. Kummerow, G. Liu, F. S. Marzano, A. Mugnai, W. Olson, G. Petty, A. Shibata, R. Spencer, F. Wentz, T. T. Wilheit, and E. Zipser, "Results of WetNet PIP-2 projects," *J. Atmos. Sci.*, vol. 55, pp. 1483–1536, 1998.

[2] F. S. Marzano, A. Mugnai, and F. J. Turk, "Precipitation retrieval from spaceborne microwave radiometers and combined sensors," in *Remote Sensing of Atmosphere and Ocean From Space*, F. S. Marzano and G. Visconti, Eds. Dordrecht, The Netherlands: Kluwer, 2002, pp. 107–126.

[3] V. Levizzani, J. Schmetz, H. J. Lutz, J. Kerkmann, P. P. Alberini, and M. Cervino, "Precipitation estimations from geostationary orbit and prospects for Metosat Second Generation," *Meteorol. Appl.*, vol. 8, pp. 23–41, 2001.

[4] M. L. Morrisey and J. E. Janowiak, "Sampling-induced conditional biases in satellite climate-scale rainfall estimates," *J. Appl. Meteorol.*, vol. 35, pp. 541–548, 1996.

[5] L. Pulvirenti, P. Castracane, F. S. Marzano, N. Pierdicca, and G. d'Auria, "A physical-statistical approach to match satellite passive microwave retrieval to the Mediterranean climatology," *IEEE Trans. Geosci. Remote Sensing*, vol. 40, pp. 2271–2284, Oct. 2002.

[6] R. V. Calheiros and I. I. Zawadzki, "Reflectivity rain-rate relationships for radar hydrology in Brazil," *J. Climate Appl. Meteorol.*, vol. 26, pp. 118–132, 1987.

[7] W. L. Crosson, C. E. Duchon, R. Raghavan, and S. J. Goodman, "Assessment of rainfall estimates using a standard Z-R relationship and the probability matching method applied to composite radar data in central Florida," *J. Appl. Meteorol.*, vol. 35, pp. 1203–1219, 1996.

[8] D. Rosenfeld, D. Atlas, and D. Short, "The estimation of convective rainfall by area integrals. Part 2: The height-area rainfall threshold (HART) method," *J. Geophys. Res.*, vol. 95, pp. 2161–2176, 1990.

[9] R. Adler, A. J. Negri, P. R. Keehn, and I. M. Hakkarinen, "Estimation of monthly rainfall over Japan and surrounding waters from a combination of low-orbit microwave and geosynchonous IR data," *J. Appl. Meteorol.*, vol. 32, pp. 335–356, 1993.

[10] C. Kummerow and L. Giglio, "A method for combining passive microwave and infrared rainfall observations," *J. Atmos. Oceanic Technol.*, vol. 12, pp. 33–45, 1995.

[11] V. Levizzani, F. Porcù, F. S. Marzano, A. Mugnai, E. A. Smith, and F. Prodi, "Investigating a SSM/I microwave algorithm to calibrate METEOSAT infrared instantaneous rain-rate estimates," *Meteorol. Applicat.*, vol. 3, pp. 5–17, 1996.

[12] F. S. Marzano, F. J. Turk, P. Ciotti, S. Di Michele, and N. Pierdicca, "Potential of combined spaceborne microwave and infrared radiometry for near real–time rainfall attenuation monitoring along earth satellite," *Int. J. Satell. Commun.*, vol. 19, no. 4, pp. 385–412, 2001.

[13] F. Richards and P. Arkin, "On the relationship between satellite-observed cloud cover and precipitation," *Mon. Weather Rev.*, vol. 109, pp. 1081–1093, 1981.

[14] P. A. Arkin and B. N. Meisner, "The relationship between large-scale convective rainfall and cold cloud cover over the Western Hemisphere during 1982," *Mon. Weather Rev.*, vol. 11, pp. 107–124, 1987.

[15] C. Kidd, "The use of passive microwave imagery in rainfall monitoring," *Remote Sens. Rev.*, vol. 42, pp. 415–450, 1990.

[16] G. Panegrossi, S. Dietrich, F. S. Marzano, A. Mugnai, E. A. Smith, X. Xiang, G. J. Tripoli, P. K. Wang, and J. P. V. Poiares Baptista, "Use of cloud model microphysics for passive microwave-based precipitation retrieval: Significance of consistency between model and measurement manifolds," *J. Atmos. Sci.*, vol. 55, pp. 1644–1673, 1998.

[17] D. M. Smith, D. R. Kniveton, and E. C. Barrett, "A statistical modeling approach to passive microwave rainfall retrieval," *J. Appl. Meteorol.*, vol. 37, pp. 135–154, 1998.

[18] G. A. Vicente, R. A. Cofield, and W. P. Menzel, "The operational GOES infrared rainfall estimation technique," *Bull. Amer. Meteorol. Soc.*, vol. 79, pp. 1883–1898, 1998.

[19] F. J. Turk, G. Rohaly, J. Hawkins, E. A. Smith, F. S. Marzano, A. Mugnai, and V. Levizzani, "Meteorological applications of precipitation estimation from combined SSM/I, TRMM, and geostationary satellite data," in *Microwave Radiometry and Remote Sensing of the Environment*, P. Pampaloni, Ed. Utrecht, The Netherlands: VSP, 1999, pp. 353–363.

[20] L. Xu, X. Gao, S. Sorooshian, P. A. Arkin, and B. Imam, "A microwave infrared threshold technique to improve the GOES precipitation index," *J. Appl. Meteorol.*, vol. 38, pp. 569–579, 1999.

[21] T. Bellerby, M. Todd, D. Kniveton, and C. Kidd, "Rainfall estimation from a combination of TRMM precipitation radar and goes multispectral satellite imagery through the use of an artificial neural network," *J. App. Meteorol.*, vol. 39, pp. 2115–2128, 2000.

[22] M. C. Todd, C. Kidd, D. Kniveton, and T. J. Bellerby, "A combined satellite passive infrared and passive microwave technique for estimation of small scale rainfall," *J. Atmos. Oceanic Technol.*, vol. 18, pp. 742–755, 2000.

[23] S. W. Miller, P. A. Arkin, and R. Joyce, "A combined microwave infrared rain rate algorithm," *Int. J. Remote Sens.*, vol. 22, pp. 3285–3307, 2001.

[24] F. S. Marzano, A. Mugnai, G. Panegrossi, N. Pierdicca, E. A. Smith, and F. J. Turk, "Bayesian estimation of precipitating cloud parameters from combined measurements of spaceborne microwave radiometer and radar," *IEEE Trans. Geosci. Remote Sensing*, vol. 37, pp. 596–613, Jan. 1999.

[25] D. Atlas, D. Rosenfeld, and D. B. Wolff, "Climatologically tuned reflectivity-rain rate relations and links to area–time integrals," *J. Appl. Meteorol.*, vol. 29, pp. 1120–1135, 1990.

[26] K. L. Hsu, X. Gao, S. Sorooshian, and H. V. Gupta, "Precipitation estimation from remotely sensed information using artificial neural networks," *J. Appl. Meteorol.*, vol. 36, pp. 1176–1190, 1997.

[27] S. Sorooshian, K. L. Hsu, X. Gao, H. V. Gupta, B. Imam, and D. Braithwaite, "Evaluation of PERSIANN system satellite-based estimates of tropical rainfall," *Bull. Amer. Meteorol. Soc.*, vol. 81, pp. 2035–2046, 2000.

[28] F. J. Turk, E. E. Ebert, B.-J. Sohn, H.-J. Oh, V. Levizzani, E. A. Smith, and R. Ferraro, "Validation of a global operational blended-satellite precipitation analysis at short time scales," in *Proc. 12th AMS Conf. Satellite Meteoroloy Oceanography*, Long Beach, CA, Feb. 13–17, 2003.

[29] F. Porcù, M. Borga, and F. Prodi, "Rainfall estimation by combining radar and infrared satellite data for nowcasting purposes," *Meteorol. Appl.*, vol. 6, pp. 289–300, 1999.

[30] C. Kidd, D. Kniveton, and C. Barrett, "The advantages and disadvantages of statistically-derived empirically-calibrated passive microwave algorithms for rainfall estimation," *J. Atmos. Sci.*, vol. 55, pp. 1576–1582, 1998.

[31] R. R. Ferraro, "SSM/I derived global rainfall estimates for climatological applications," *J. Geophys. Res.*, vol. 102, pp. 16 715–16 735, 1997.

[32] G. W. Petty, "The status of satellite-based rainfall estimation over land," *Remote Sens. Environ.*, vol. 51, pp. 125–137, 1995.

[33] W. Berg, W. Olson, R. Ferraro, S. J. Goodman, and F. J. LaFontaine, "An assessment of the first-and second-generation of navy operational precipitation retrieval algorithms," *J. Atmos. Sci.*, vol. 55, pp. 1558–1575, 1998.

[34] L. J. Crone, L. M. McMillin, and D. S. Crosby, "Constrained regression in satellite meteorology," *J. Appl. Meteorol.*, vol. 35, pp. 2023–2039, 1996.

[35] F. S. Marzano, E. Fionda, P. Ciotti, and A. Martellucci, "Ground-based multi-frequency microwave radiometry for rainfall remote sensing," *IEEE Trans. Geosci. Remote Sensing*, vol. 40, pp. 742–759, Apr. 2002.

[36] L. Xu, S. Sorooshian, X. Gao, and H. V. Gupta, "A cloud-patch technique for identification and removal of no-rain clouds from satellite infrared imagery," *J. Appl. Meteorol.*, vol. 38, pp. 1170–1181, 1999.

[37] M. B. Ba and A. Gruber, "GOES multispectral rainfall algorithm," *J. Appl. Meteorol.*, vol. 40, pp. 1500–1514, 2001.

[38] D. Rosenfeld and I. M. Lensky, "Satellite-based insights into precipitation formation processes in continental and maritime convective clouds," *Bull. Amer. Meteorol. Soc.*, vol. 79, pp. 2457–2476, 1998.

IEEE TRANSACTIONS ON GEOSCIENCE AND REMOTE SENSING, VOL. 42, NO. 5, MAY 2004

[39] Y. C. Hong, C. D. Kummerow, and W. S. Olson, "Separation of convective and stratiform precipitation using microwave brightness temperature," *J. Appl. Meteorol.*, vol. 38, pp. 1195–1213, 1999.

[40] R. F. Adler and A. J. Negri, "A satellite infrared technique to estimate tropical convective and stratiform rainfall," *J. Appl. Meteorol.*, vol. 27, pp. 30–51, 1988.

[41] F. J. Turk, S. W. Bidwell, E. A. Smith, and A. Mugnai, "Investigating inter-satellite calibration for the GPM era," in *Proc. 12th AMS Conf. Satellite Meteoroloy Oceanography*, Long Beach, CA, Feb. 13–17, 2003.

Frank Silvio Marzano (S'89–M'99–SM'03) received the laurea degree (cum laude) in electrical engineering and the Ph.D. degree in applied electromagnetics, in 1988 and 1993, respectively, both from the University "La Sapienza," Rome, Italy.

He currently teaches a course on antennas and propagation and coordinates the satellite and radar remote sensing group within the Center of Excellence (CETEMPS) in the Department of Electrical Engineering, University of L'Aquila, L'Aquila, Italy. In 1993, he collaborated with the Institute of Atmospheric Physics (CNR), Rome, Italy. From 1994 until 1996, he was with the Italian Space Agency, Rome, Italy, as a Post-Doctorate Researcher. After being a Lecturer at the University of Perugia, Perugia, Italy, in 1997, he joined the Department of Electrical Engineering, University of L'Aquila. His current research interests are passive and active remote sensing of the atmosphere from ground-based, airborne, and spaceborne platforms, with a particular focus on precipitation using microwave and infrared data, development of inversion methods, radiative-transfer modeling of scattering media, and scintillation and rain-fading analysis along satellite microwave links.

Dr. Marzano received the Young Scientist Award of the XXIV General Assembly of the International Union of Radio Science in 1993. In 1998, he was the recipient of the Alan Berman Publication Award from the Naval Research Laboratory, Washington, DC.

Massimo Palmacci received the laurea degree in electronic engineering from the University of L'Aquila, Italy, in 2000.

Since 2001, he has been with a private company, working on radar systems. He is currently a Research Collaborator with the Center of Excellence (CETEMPS), University of L'Aquila, L'Aquila, Italy, where he is focused on satellite meteorology topics.

Domenico Cimini (M'03) was born in Teramo, Italy, in 1973. He received the M.S. (cum laude) and Ph.D. degrees from the University of L'Aquila, L'Aquila, Italy, in 1998 and 2002, respectively, both in physics.

Between 1999 and 2001, he spent 18 months with the Environmental Technology Laboratory (ETL), National Oceanic and Atmospheric Administration (NOAA), Boulder, CO, working on radiometer calibration techniques, remote sensing of the ocean surface, and microwave radiative transfer model comparisons. During this period, he was a Guest Scientist with the Water Vapor Intensive Operational Period (WVIOP2000), at the Atmospheric Radiation Measurement (ARM) program Southern Great Plain (SGP) site in Lamont, OK. He is currently with the Remote Sensing Division, Center of Excellence (CETEMPS), University of L'Aquila, where he is working on ground- and satellite-based passive microwave and infrared radiometry.

Graziano Giuliani received the laurea degree in physics from the University of Rome "La Sapienza," Italy, in 1997.

He has worked for a private company on designing and coding satellite data management software before coming back to research tasks at the Scientific and Technologic Park of Abruzzo (PSTA), L'Aquila, Italy. Since 2002, he has been a Research Fellow with the Department of Electrical Engineering and the Center of Excellence (CETEMPS), University of L'Aquila, Italy.

Francis Joseph Turk (A'80–S'91–M'91) was born in Hibbing, MN, on August 25, 1960. He received the B.S. and M.S. degrees in electrical engineering from Michigan Technology University, Houghton, in 1982 and 1984, respectively, and the Ph.D. degree from Colorado State University (CSU), Fort Collins, in 1991.

From 1984 to 1986, he was with the Communications Group at Motorola Inc., Schaumberg, IL, where he worked on the development of cellular mobile telephones. From 1986 to 1990, he was an Army Center for Geosciences Fellow at CSU, where his research focused upon passive microwave radiometry, microwave radiative transfer, and polarimetric radar applied to satellite remote sensing of precipitation. His additional research areas have particle scattering theory and atmospheric radio propagation. In 1995, he joined the Marine Meteorology Division of the Naval Research Laboratory, Monterey, CA, where he is involved in the analysis and applications of polar and geostationary meteorological satellite data for naval forecasting and advanced cloud products, data assimilation into numerical weather prediction models, and radiative transfer modeling of clouds and gases.